International Journal of Refrigeration 161 (2024) 188–201

Contents lists available at ScienceDirect

International Journal of Refrigeration

journal homepage: www.elsevier.com/locate/ijrefrig

A homogeneous relaxation model algorithm in density-based formulation with novel tabulated method for the modeling of CO_2 flashing nozzles

Algorithme de modèle de relaxation homogène dans une formulation basée sur la masse volumique avec une nouvelle méthode tabulée pour la modélisation des tuyères à jet de CO_2.

Antoine Metsue [*,a,b], Sébastien Poncet [b], Yann Bartosiewicz [a]

[a] Institute Mechanics, Materials, and Civil Engineering (iMMC), Université catholique de Louvain (UCLouvain), 1348, Louvain-la-Neuve, Belgium
[b] Mechanical Engineering Department, Université de Sherbrooke, 2500 boulevard de l'Université, Sherbrooke. (QC) J1K 2R1, Canada

ARTICLE INFO

Keywords:
Carbon dioxide
Metastability
Homogeneous equilibrium model
Homogeneous relaxation model
Tabulated equation of state
SU2 solver
Wall-resolved modeling

Mots clés:
Dioxyde de carbone
Métastabilité
Modèle d'équilibre homog..ne
Modèle de relaxation
Équation d'état tabulée
Solutionneur SU2

ABSTRACT

Accurate prediction of the flow physics within nozzles and ejectors working with two-phase carbon dioxide remains particularly challenging. Indeed, the flashing phenomenon in the device often comes along with the formation of the metastable phase, which can severely affect both the flow physics, and the flow rate. Due to the particular challenges associated with building and operating two-phase carbon dioxide experimental setups, computational fluid dynamics constitutes a compelling alternative to study and predict nozzle and ejector flows. In this work, the metastability effects are modeled through a Homogeneous Relaxation Model for the first time expressed in density-based formulation, within the SU2 solver. The thermodynamic relations for the equation of state are tabulated using a novel quad-tree algorithm and directly coupled to the solver, ensuring fast and accurate predictions. The simulation tool is then validated against experimental nozzle pressure profiles and used to compare the commonly used Homogeneous Equilibrium Model to the Homogeneous Relaxation Model in terms of local flow topology and mass flow rates. Most notably, it was found that the Homogeneous Relaxation Model was able to better fit the experimental pressure profiles within the first part of the expansion.

1. Introduction

Carbon dioxide (CO_2) has emerged as a suitable alternative to conventional refrigerants owing to its minimal impact on climate change. With a noteworthy combination of attributes, including a zero ozone depletion potential (ODP) and a global warming potential GWP = 1, CO_2 has garnered substantial attention from the industry. Particularly in the context of refrigeration and heat pump systems, CO_2 stands out as an attractive working fluid due to its non-toxic and non-flammable nature, adding to the fact that transition towards CO_2 utilization has been necessitated by international agreements such as the Kyoto Protocol, which outlined phased reductions in the usage of Hydro-ChloroFluoroCarbons (HCFCs) by 2020–2030 and HydroFluoroCarbons (HFCs) by 2025–2040 (Abas et al., 2018). More recently, the European Commission reviewed the F-gas regulation with the intent to reduce the EU's fluorinated greenhouse gases emissions by two thirds by 2030.

The particular thermodynamic properties of CO_2, with a critical temperature of 31 [°C], require the operation of the cycle under transcritical conditions. However, it introduces considerable losses in the expansion valve due to the high pressure ratio (Kim et al., 2004) and the entropy production during the isenthalpic expansion. Devices such as ejectors are then the subject of many researches, as they can be used to partially recover the expansion losses into useful mechanical work. Nonetheless, ejectors are notoriously characterized by complex fluid dynamics, and some of the underlying mechanisms within these devices remain insufficiently understood, impeding overall system performance (Besagni, 2019). One particular aspect adding to this complexity is the emergence of the metastable phase during the flashing of the flow within the primary nozzle of the ejector. In such highly compressible flows, the phase change significantly depends on the rate of bubble nucleation (Quinn et al., 2022); the decompression is so fast, inducing high

* Corresponding author.
E-mail address: antoine.metsue@uclouvain.be (A. Metsue).

https://doi.org/10.1016/j.ijrefrig.2024.02.020
Received 3 December 2023; Received in revised form 1 February 2024; Accepted 17 February 2024
Available online 23 February 2024
0140-7007/© 2024 Elsevier Ltd and IIR. All rights reserved.

Nomenclature

Alpha numeric symbols

e	Specific energy $[J.kg^{-1}]$
h	Specific enthalpy $[J.kg^{-1}]$
k	Turbulence kinetic energy $[J.kg^{-1}]$
p	Pressure $[Pa]$
q	Heat flux $[J.m^{-2}.s^{-1}]$
s	Specific entropy $[J.kg^{-1}.K^{-1}]$
T	Temperature $[K]$
t	Time $[s]$
u	Velocity $[m.s^{-1}]$
v	Specific volume $[m^3.kg^{-1}]$
x	Quality [-]
z	Spatial coordinate $[m]$

Greek letters

α	Void fraction [-]
κ	Thermal conductivity $[W.m^{-1}.K^{-1}]$
ω	Specific dissipation rate $[s^{-1}]$
ρ	Density $[kg.m^{-3}]$
θ	Relaxation time $[s]$

Subscripts

c	Critical point
eq	Equilibrium
in	Inlet
ml	Metastable liquid
sat	Saturation conditions
sv	Saturated vapor
t	Total conditions

velocities and low residence time, that the fluid does not have sufficient time to reach equilibrium and then vaporize under the usual saturation conditions. Consequently, there is a delay before the flow returns to the liquid-vapor equilibrium state. This practical implication results in distinct flow topologies, thermodynamic states, and higher mass flow rates than equilibrium conditions. Addressing, predicting and understanding these aspects is then crucial to correctly model two-phase CO_2 ejectors, as the correct modeling of the primary stream issued from the nozzle is the key to further predict the correct entrainment capability of the ejector.

Design of nozzles and ejectors is often achieved using numerical tools. Thermodynamic models are fast and allow to predict the operation of the device for a wide range of conditions to determine the main geometric parameters. The design can then be refined through a Computational Fluid Dynamics (CFD) analysis that also allows access to local flow features. It enables a deeper analysis of the influence of the geometry on the device's operation. Experimental campaigns, despite being associated with challenges related to high pressures (within the range 50 - 100 [bar]) and small dimensions of the components (nozzle diameter of about 1 [mm]), are then necessary in order to calibrate 1D models and validate the CFD results. Reynolds-Averaged Navier-Stokes (RANS) models for incompressible (or weakly compressible) flows and Favre-Averaged Navier-Stokes (FANS) models for compressible flows are statistically averaged models that rely on a turbulence closure scheme. Because of the prohibitive computation times associated to direct or large eddy simulations, most two-phase nozzle and ejector simulations performed up to now are based on RANS or FANS closures. Most studies that have been undertaken to perform CFD of two-phase CO_2 ejectors (Giacomelli et al., 2019; 2016; Haida et al., 2018; Palacz et al., 2017) were done using the commercial software `ANSYS Fluent` (ANSYS, 2023), using a pressure-based solver. However, as pointed out by Fang (2019), *density-based* flow solvers are more suitable for computing compressible flows.

As underlined by Ringstad et al. (2020), accurate multiphase flow modeling is generally considered as the most challenging aspect and the key factor for successful modeling of CO_2 ejectors. Complex interactions take place between the vapor and liquid phases, adding to the fact that the flow flashes into the primary nozzle in the case of transcritical CO_2 operation. There are several model hierarchies to handle two-phase flows according to the type of equilibrium (mechanical, thermal, chemical) that is assumed to be relaxed (De Lorenzo, 2018). One can distinguish pseudo fluids, for which the equations of both phases are averaged into one set of the mixture equations, from proper two-fluid models where one set of equations is solved for each phase. The widely adopted approach, known as the *Homogeneous Equilibrium Model* (HEM), characterizes the flow as a pseudo fluid in mechanical, thermodynamic and chemical equilibria. More sophisticated approaches include the *Homogeneous Relaxation Model* (HRM) or the *Delayed Equilibrium Model* (DEM), that are so-called 4-equation models that assume only mechanical equilibrium (Ringstad et al., 2020). The HEM has been extensively used to model CO_2 ejector flows (Fang et al., 2019; Liu et al., 2012; Lucas et al., 2014; Palacz et al., 2015; Ringstad et al., 2020; Smolka et al., 2013) as it provides a simplistic approach toward two-phase flow modeling. This allows to define the state of the vapor-liquid mixture with only two independent parameters. Palacz et al. (2015) investigated the accuracy of the HEM depending on the operating conditions of the CO_2 ejector. It was found that the HEM could accurately predict mass flow rates for primary nozzle conditions close or above the critical point (i.e., for tested conditions with pressures between 70 and 95 [bar] and temperatures between 25 and 35 [°C], roughly), with a relative error inferior to 10%. However, the accuracy of the HEM quickly drops as the motive temperature decreases, reaching motive mass flow rate discrepancies up to 59.43%. Those errors were attributed to metastability effects that are not taken into account by the HEM. Metastability effects should be most present as the inlet temperature gets lower since the expansion path is expected to cross the saturation curve at lower pressures, where the range of possible metastable states is larger.

Building on the conclusion drawn by Palacz et al. (2015), metastability effects should be taken into account for the modeling of flashing ejectors with low inlet temperatures. To do so, an additional transport equation for the vapor fraction with a phase change model is needed (Ringstad et al., 2020). As the DEM is mostly limited to 1D simulations since it requires a 1D semi-empirical relation to model the saturated mass fraction evolution along the direction of the expansion, the HRM constitutes a compelling approach for modeling metastability. Initially proposed by Bilicki et al. (1990), the HRM diverges from the instantaneous equilibrium assumption made in HEM and treats phase change as a relaxation process towards the equilibrium vapor quality. Downar-Zapolski et al. (1996) presented a correlation for the relaxation time and validated it in the case of flashing water. Angielczyk et al. (2010) extended the closure law for CO_2. Their 1D HRM results were compared to available experimental nozzle data (Nakagawa et al., 2009) and a reasonable agreement was found downstream of the throat. Haida et al. (2018) later investigated the performance of the HRM and deduced correlations for the relaxation time for CO_2 from genetic algorithm optimization, and three operating ranges were defined according to the motive nozzle pressure, in order for the related set of empirical coefficients to minimize the discrepancy between CFD and experimental results. Recently, the HRM was used in 1D by Log et al. (2024a,b) to study non equilibrium effects within CO_2 pipe depressurization.

Another important aspect of any CFD simulation is the equation of

state (EoS) used to compute fluid properties at vapor, liquid, supercritical, two-phase equilibrium and metastable states. The work of Raman and Kim (2018) has demonstrated that the computation of these properties can significantly influence CFD results. However, it is essential to ensure that the computation time for the EoS remains reasonable. De Lorenzo et al. (2017) identified three approaches to achieve this goal: using a simple EoS, employing an iterative algorithm with an accurate EoS, or utilizing tabulated methods. Smolka et al. (2013) presented a model of the compressible transonic single- and two-phase flow of a real fluid within an ejector. The authors validated their model using the perfect gas (PG) EoS, both for single-phase refrigerants and for two-phase CO_2 even though the PG EoS is not suited for predicting such complex mixtures (Fang et al., 2018). Another alternative is the Peng-Robinson (PR) EoS, used by Brown et al. (2014) to simulate high pressure CO_2 pipelines. Note however that the PR EoS is not suitable for the simulation of two-phase flows such as flashing CO_2 nozzles, as it is invalid under the saturation dome since this EoS predicts negative speeds of sound in this region (Fang, 2019). The currently most accurate EoS for CO_2 is the Span-Wagner (SW) EoS (Span and Wagner, 1996). It is based on hundreds of parameters fitted using extensive experimental data. It has been implemented into thermophysical property libraries like `REFPROP` (Lemmon et al., 2010) and `COOLPROP` (Bell et al., 2014). Despite its high accuracy, the SW EoS requires considerable computational resources, leading to the preference for tabulated EoSs. With those methods, the time-consuming iterative procedure for the EoS is usually performed at the beginning of the computation to create a table that will be used in the later stages of the simulation, by interpolating the tabulated values. Giacomelli et al. (2016) constructed lookup tables in the (specific volume - specific internal energy) space from `REFPROP` using an in-house `Matlab` code, to perform ejector simulations with `ANSYS Fluent`. The authors implemented a bi-linear interpolation scheme to retrieve the adequate values of density and speed of sound at each cell of the domain. Ameli et al. (2017) later implemented a similar lookup table in `FORTRAN` and coupled it to `ANSYS CFX 17.0` to investigate the condensation process in transcritical CO_2 nozzles. Fang et al. (2018) developed a similar `FORTRAN` lookup table for CO_2 by adapting the work of De Lorenzo et al. (2017) for water. The tabulated method used bilinear interpolation and had a speed-up factor of about 66 compared to the original SW EoS. Later, Föll et al. (2019) developed a tabulated method based on piecewise polynomials with adaptive refinement in the state space and coupled it to the `FORTRAN` CFD solver `FLEXI` (Flexi, 2023). Lastly, Rubino et al. (2018) developed a lookup table based on unstructured grids with mesh refinement. Their method based on a bilinear interpolation scheme was coupled to the non-ideal CFD `SU2` solver. They found out that an unstructured interpolation grid was beneficial in terms of computation time only when it was coarse enough.

To the best of the authors' knowledge, none of the aforementioned 2D RANS studies on HRM used a density-based solver though it is more appropriate for highly compressible flows (Fang, 2019). This is most likely because the HRM is favorable to a pressure-based implementation, as discussed in the following sections. Moreover, the literature often lacks of comprehensive explanations about the computation of metastable properties, including limitations related to the spinodal limit, that is, the limit beyond which the fluid becomes unstable (phase change must happen before reaching this limit). In this study, one introduces two novel tools for CFD modeling of compressible two-phase flows. First, a new general EoS tabulation algorithm is presented. The tabulated method combines for the first time a piecewise bicubic interpolation of the thermodynamic properties with local refinement of the interpolation grid based on a required accuracy. Secondly, a HRM is implemented within the `SU2` solver (Palacios et al., 2013) and directly coupled to the FANS solver. This implementation represents the first instance of expressing the HRM in a density-based formulation. To validate and verify non-equilibrium phenomena within flashing CO_2 devices, good quality (CFD-grade) local measurements are needed. However, there is a clear lack of experimental data available for relevant cases (nozzles or ejectors with low inlet temperatures, that should be desired in refrigeration applications). The standard cases of Nakagawa et al. (2009) despite lacking mass flow measurements, constitute, to the best of the authors' knowledge, the only set of data that is suitable to study/-validate the effects of metastability within the flashing CO_2 nozzle. In this work, wall-resolved simulations of the cases of Nakagawa et al. (2009) are then performed using both the HEM and the newly implemented HRM to investigate and compare their predictive capabilities with respect to metastability phenomena.

2. Numerical methodology

In this section, all ingredients of the numerical solver are detailed. This includes geometrical modeling, multiphase models (HEM and HRM), the lookup table construction and interpolation methods to evaluate the thermodynamic properties, initial and boundary conditions, the calculation procedures and the mesh grid.

2.1. Geometrical modeling and operating conditions

The present study is performed using the classical cases of Nakagawa et al. (2009), who considered the discharge of high pressure CO_2 through four different 2D (rectangular, with a width of 3 [mm]) nozzle geometries, that differ only by the angle of the divergent section θ. The dimensions and operating conditions of the devices are given in Table 1, and the nozzle schematic along with the mesh is shown in Fig. 1. Although four geometries were presented in Nakagawa et al. (2009), the geometry with the highest diverging angle is discarded here. The reason is that, for such a configuration, the solid phase is present in the nozzle (the pressure falls below the triple point pressure during the CFD). Note that even though the geometry is 2D, 3D effects are still to be expected in the experiment, which may be the cause of some discrepancies with numerical results (Lamberts, 2018).

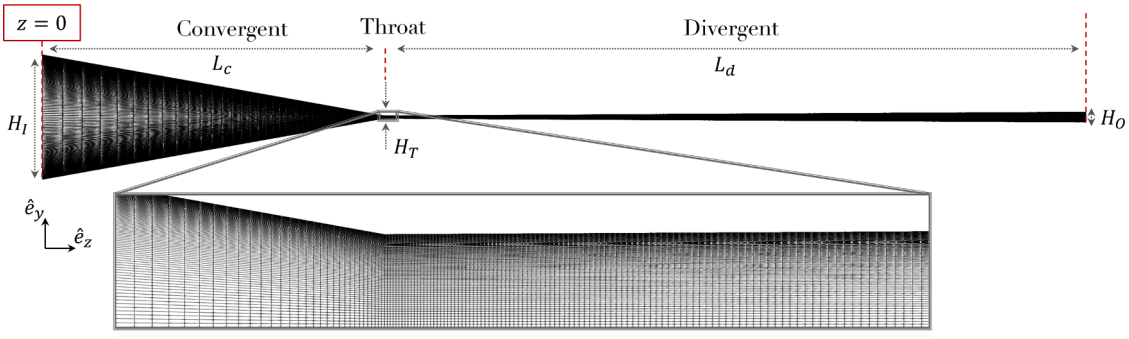

Fig. 1. Two-dimensional mesh for the nozzle case c of Nakagawa et al. (2009) with relevant notations. The related dimensions for the different geometries are given in Table 1.

Table 1
Dimensions and operating conditions of the nozzles considered by Nakagawa et al. (2009).

Nozzle	p_{in} [MPa]	T_{in}[°C]	θ[°]	H_o [mm]	H_T [mm]	H_I [mm]	L_c [mm]	L_d [mm]
a	6.1	20.5	0.076	0.39	0.24	10	27.35	56.15
b	6.1	20	0.153	0.54	0.24	10	27.35	56.15
c	6.1	21.8	0.306	0.84	0.24	10	27.35	56.15

2.2. Numerical modeling

The FANS simulations are performed with the open-source *real-gas* SU2 (version 7.3.1) solver. The partial differential equations (PDEs) in SU2 are discretized using a finite volume method with a standard edge-based structure on a dual grid with control volumes constructed using a median-dual, vertex-based scheme. For detailed information, the interested reader is invited to refer to Palacios et al. (2013), where the FANS equations are also presented. The main numerical aspects of the code along with the particular setup used in the present work are however described in this section.

As the solver is density-based, the solution variables are (ρ, ρu_j, ρe_t) with ρ the density and u the velocity, with the j subscript referring to the three spatial directions. The total energy e_t is defined as:

$$e_t = e + \frac{u_j u_j}{2} + k, \tag{1}$$

where the t subscript indicates total quantities and k is the turbulence kinetic energy (TKE). The Menter Shear Stress Transport model (Menter, 1994) ($k-\omega$ SST) is used, as it demonstrated good agreement with experimental measurements, for both local and global flow quantities in the case of perfect and real gas ejector flows (Croquer et al., 2016; Lamberts et al., 2018).

In the present work, the convective fluxes are integrated using the classical Roe scheme (Roe, 1981) with second order reconstruction. The gradients of the flow variables required for the computation of the viscous fluxes are calculated using a Green-Gauss method. For the HEM, an implicit Euler time integration scheme is employed, where the steady-state solver uses local time-stepping in order to accelerate the convergence. Note that by doing so, the intermediate results of the FANS simulation have no physical meaning, but the converged steady-state solution does. For the HRM, the explicit Euler scheme is used for pseudo-time integration. This is because the implicit formulation requires complex thermodynamic derivatives and complex modifications in the solver that are beyond the scope of the current work.

2.3. Multiphase modeling

In the following, the Homogeneous Relaxation Model (HRM) is described and its differences with respect to the Homogeneous Equilibrium Model (HEM) are highlighted.

In the HEM, both mechanical and thermodynamic equilibria between phases are assumed. Consequently, using the HEM is equivalent to considering that both phases exchange mass instantaneously (through evaporation and condensation), or in other words, that the equilibrium of the phases is reached instantaneously. In practice, this hypothesis may not be true as mass exchange processes require some time to take place, and as the flow is highly compressible, the time scale of said processes may become of the same order of magnitude as the time scale of the expansion process. It is then expected that a metastable phase may appear (for example, the metastable *liquid* phase in a flashing nozzle), which could influence the flow physics in a non negligible manner. As the HEM is not able to model metastability, one may add an extra equation for the transport of the vapor phase and model the delay to reach equilibrium as a relaxation process. This approach constitutes the basis of the HRM, that belongs to the family of 4-equation models (please refer to De Lorenzo (2018) for additional details). In the HRM, the mechanical equilibrium of the two phases is kept (i.e., same pressure and velocity), but the thermodynamic equilibrium is relaxed. In practice, the fluid is then modeled as a mixture of saturated vapor and metastable liquid, and the temperature equality of the two phases is not assumed like in HEM. The additional equation needed to solve the saturated vapor phase is then modeled as:

$$\frac{\partial}{\partial t}(\alpha\rho_{sv}) + \frac{\partial}{\partial z_i}(\alpha\rho_{sv}u_i) = \Gamma, \tag{2}$$

with α the void fraction and Γ a phase source term. The above relation can be obtained by writing the mass conservation equation for the vapor phase over a control volume, using the definition of the void fraction $\alpha = \frac{\rho_l-\rho}{\rho_l-\rho_{sv}} = \frac{\rho x}{\rho_{sv}}$, with the l subscript referring to the liquid phase (metastable or saturated). Using the latter relation, Eq. (2) can be written in terms of quality as:

$$\frac{\partial}{\partial t}(\rho x) + \frac{\partial}{\partial z_i}(\rho u_i x) = \Gamma. \tag{3}$$

The source term Γ is then required to allow mass transfer between the two phases, as $\Gamma = 0$ implies pure convection of the phases. For the HRM, Γ models a relaxation process towards the equilibrium state:

$$\Gamma = -\rho\frac{x - x_{eq}}{\theta}, \tag{4}$$

where x_{eq} is the equilibrium quality and θ is the relaxation time. The latter was modeled by Downar-Zapolski et al. (1996) as:

$$\theta = \theta_0 \alpha^a \Phi^b, \tag{5}$$

where θ_0 is the initial relaxation time, a and b are empirical coefficients and Φ is the non-dimensional pressure difference. Angielczyk et al. (2010) extended the formulation of θ, initially validated in the case of water, to flashing CO_2. Additionally, the same authors (Angielczyk et al., 2010) extended the definition of Φ to handle supercritical inlet conditions by computing the latter as a function of the inlet entropy instead of the temperature as in the work of Downar-Zapolski et al. (1996):

$$\Phi = \left|\frac{p_{sat}(s_{in}) - p}{p_c - p_{sat}(s_{in})}\right|, \tag{6}$$

with p_c the critical pressure and s_{in} the inlet entropy. In the following, constant θ values will be first considered to perform a parametric analysis. Then, the correlation of Angielczyk et al. (2010) with ($\theta_0 = 2.14 \times 10^{-7}$ [s], $a = -0.54$, $b = -1.76$) will be applied. Note that an alternative formulation for the relaxation time was recently proposed by Log et al. (2024a), but is was found that the values of θ obtained with this method were high and could not be applied in the present case as the spinodal limit would be reached.

As mentioned in the previous section, the HRM is favorable for a pressure-based implementation of the RANS solver. In that case, the pressure is a solution variable and it can be used directly to recompute the two-phase mixture density, as per, e.g., (Haida et al., 2018; Palacz et al., 2017), using the following mixture equations:

$$\frac{1}{\rho} = \frac{x}{\rho_{sv}(p)} + \frac{1-x}{\rho_{ml}(p, h_{ml})}, \qquad \mathrm{h} = \mathrm{x}h_{sv}(p) + (1-x)h_{ml} \tag{7}$$

with the $_{ml}$ subscript referring to the metastable liquid phase. Although the exact manner in which Eq. (7) are used is not well described in the literature, it is assumed that the enthalpy equation is inverted to

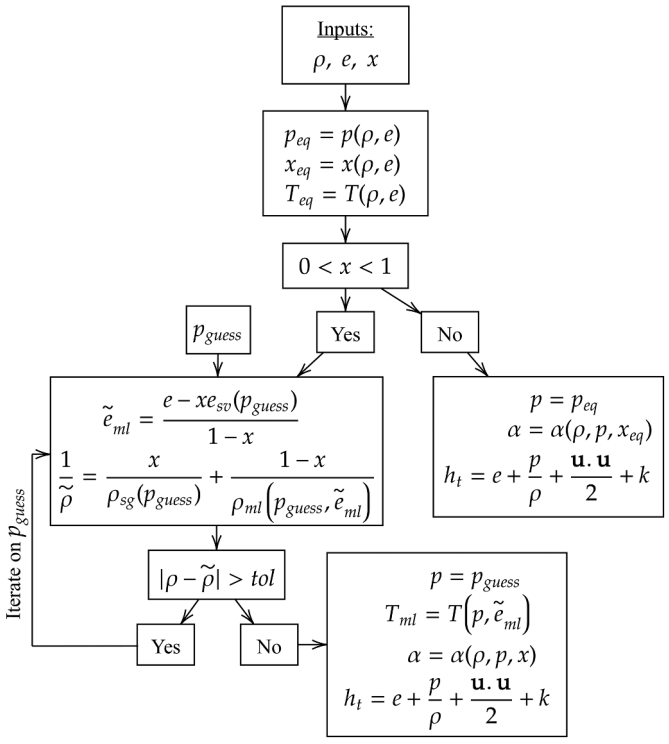

Fig. 2. Flowchart of the HRM algorithm in density-based formulation.

compute h_{ml} from solution variables (p, u_i, x, h_t), which is in turn used to compute the density.

Because the present solver –SU2– is *density-based*, the same algorithm cannot be used to apply the HRM. Indeed, in this case, the density is now a solution variable, which should not be re-computed as this would lead to incoherence in the modified FANS equations. Instead, the proper way to solve this problem is to compute the pressure and total enthalpy as functions of the solution variables $(\rho, \rho u_i, \rho x, \rho e_t)$. However, because saturation properties are computed as functions of pressure, which is to be calculated from solution variables, one must iterate on that said pressure to find the solution. Fig. 2 illustrates the proposed algorithm for a density-based solver. The procedure to compute the state begins with the input of (ρ, e, x) that are either solution variables or easily computed from those. The equilibrium quantities (same as HEM) are first computed, then if the state is under the saturation dome, the HRM algorithm is used, otherwise the pressure is equal to the equilibrium pressure, that is then used to compute the total enthalpy. If two-phase is detected, the closure equations for the specific energy and the density are solved by iterating on the pressure until sufficient precision is met. In practice, a golden search-type method is used to converge on the solution pressure, with the triple and critical pressures of CO_2 as lower and upper bounds, respectively. Once the solution pressure is found, the remaining properties such as the metastable temperature T_{ml}, void fraction α and total specific enthalpy h_t can be retrieved directly. Note that the conduction term has then to be divided in two terms, weighted by the void fraction, to account for the contributions from both the saturated vapor and metastable liquid phases:

$$q = -(1-\alpha)\kappa_{ml}\frac{\partial T_{ml}}{\partial z_j} - \alpha\kappa_{sv}\frac{\partial T_{sv}}{\partial z_j}. \tag{8}$$

2.4. Tabulated method

The EoS used in the present work is provided by the `REFPROP`/`COOLPROP` libraries which implement the SW EoS. As the `SU2` solver was made suited to handle real-gas CFD, the state is contained within a `Fluid` object and the EoS is implemented in the related `Fluid` class.

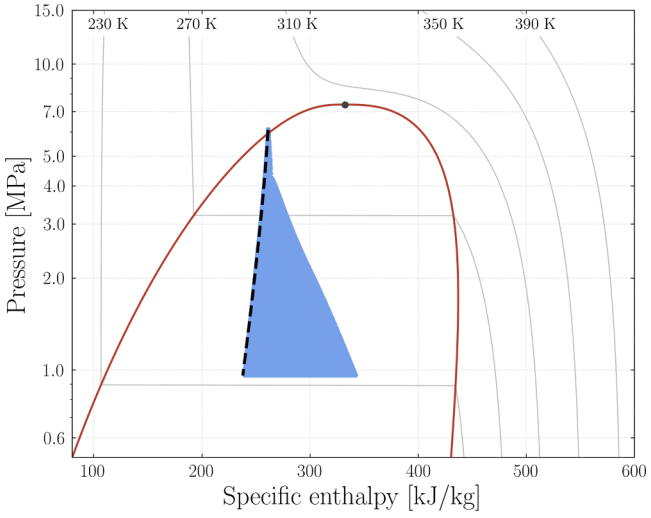

Fig. 3. Range of operation (in blue) of the nozzle of Nakagawa et al. (2009) (case c, see Table 1). The saturation dome is highlighted in red with the critical point marked with the black dot. The dashed curve is the isentropic expansion, for reference.

The thermodynamic relations required by the solver must then be implemented. In this case, since the solver is density-based, the relation needed for closure is of the type $\chi = \chi(\rho, e)$, where χ is any relevant thermodynamic property. Depending on the desired features of the solver, thermodynamic relations are also required in state spaces different than $(\rho - e)$, e.g., in $(p - T)$ and $(h - s)$ state spaces for the computation of total boundary conditions, or even in $(p - e_{ml})$ to compute the metastable liquid density in HRM (Fig. 2).

The table is generated by a Python routine and the properties are retrieved through the Python wrapper for `COOLPROP`, that offers a `REFPROP` interface as well. By default, the properties are retrieved from `REFPROP` except in the case of the thermodynamic derivatives (mostly required for the implicit Euler integration scheme), that are only available in `COOLPROP`. These derivatives are however limited to the single-phase region and two-phase properties must be reconstructed from the saturation properties as done by Fang (2019).

2.4.1. Look-up table boundaries

Since the present lookup tables are generated with the aim of performing CFD of transcritical CO_2 nozzles, the state space boundaries are chosen to enclose the range in which those devices should operate. However, it is necessary to provide some margins because the numerical solver can oscillate during the solution convergence process. Fig. 3 displays the $p - h$ diagram of CO_2 in which the blue area represents the range of states that are found in the nozzle of Nakagawa et al. (2009) (case c, Table 1). Those states were obtained by performing the RANS simulation in `SU2` using the HEM. The theoretical isentropic expansion curve is also plotted as a reference. For this work, the table boundaries were represented in the $p - h$ diagram because it offers good readability for applications in refrigeration cycles and is easy to interpret compared to less usual diagram such as the $\rho - e$ diagram. The bottom/top boundaries were chosen as 0.52/50 [MPa] (the low pressure corresponds to the triple point pressure). The left boundary is then the enthalpy of the triple point whereas the right boundary corresponds to the enthalpy at 800 K and the lowest pressure. Those boundaries apply for all tables, whether the state space is $\rho - e$ or another one. The method is however not restricted to such kind of boundaries and the user is free to implement new ones.

2.4.2. Interpolation method

A bicubic interpolation scheme is implemented in the state space, as it was found that this method allows good precision whilst requiring

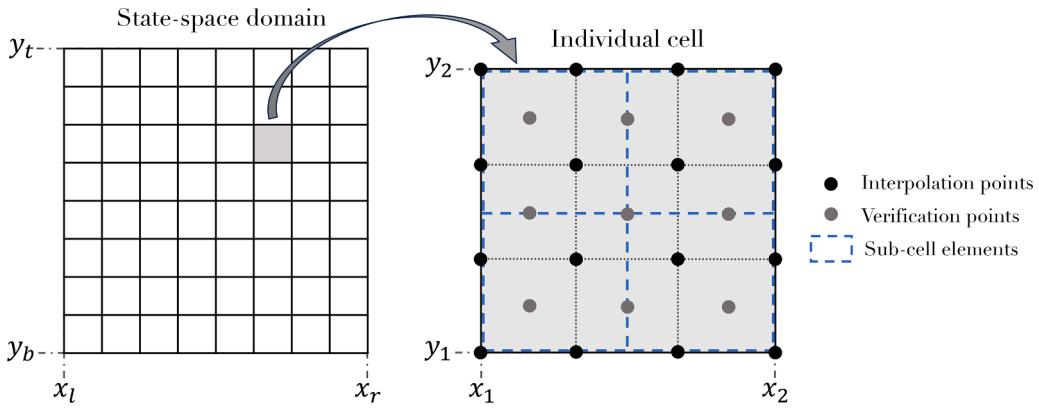

Fig. 4. Schematic of an individual cell taken in the state-space domain. The thermodynamic relation is interpolated on 16 equally-spaced points and the error is calculated at 9 locations called verification points.

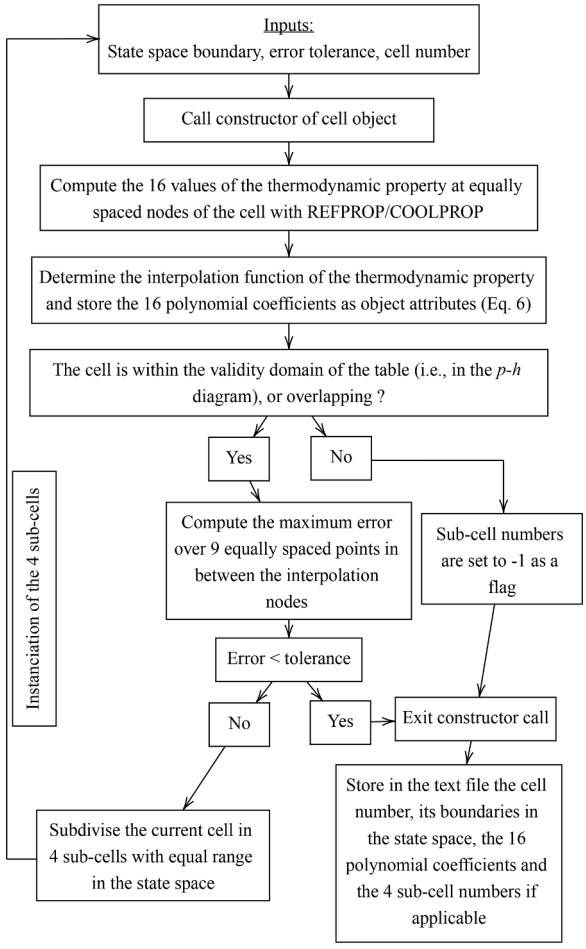

Fig. 5. Flowchart of the grid generation algorithm for the look-up table.

limited memory storage compared to more complex approximation methods, or even the simpler bilinear interpolation. Indeed, a bicubic function reduces the amount of required cell elements by two orders of magnitude while requiring only 4 times more memory per cell, compared to a bilinear function.

The state space is discretized by a number of rectangular cells until a given absolute interpolation precision is reached for the required thermodynamic variable. The mesh generation algorithm in the state space is described in the following. Fig. 4 displays a schematic of a cell element taken from the state space whose boundaries ($x_{l,r}$, $y_{b,t}$) are set as inputs by the user. Each cell is defined by its boundaries in ($x_{1,2}$, $y_{1,2}$) and the values at the 16 equally spaced nodes (black dots in the figure) are evaluated to calculate the bicubic polynomial:

$$F = XAY, \tag{9}$$

where X is the 4×4 matrix where each line is of the form $[1, x_i, x_i^2, x_i^3]$, with the i subscript ranging from 1 to 4, which corresponds to the abscissa of the 16 passage points (Fig. 4). Matrix Y is reciprocally the same for the ordinate but transposed, and $F_{ij} = f(x_i, y_j)$ is the evaluation of the thermodynamic function. The 16 polynomial coefficients A_{ij} can then be retrieved by matrix inversion:

$$A = X^{-1} F Y^{-1}. \tag{10}$$

To speed up the generation process and avoid a loss in accuracy (due to finite machine precision) for large values of (x, y), the cell boundaries are normalized, thereby, $X^{-1} = (Y^{-1})^T$ is constant.

During the CFD simulation, the 16 coefficients of A are retrieved from the look-up table and the thermodynamic property is computed. Note that the coordinates in the state space (x^*, y^*) must also be normalized by the cell dimensions, i.e.,

$$x^* = \frac{x - x_1}{x_2 - x_1} \qquad y^* = \frac{y - y_1}{y_2 - y_1}. \tag{11}$$

2.4.3. *Mesh generation algorithm*

A local refinement method is implemented in the thermodynamic state space in order to limit the storage required for the interpolated quantities. In this way, more elements are generated where the function is strongly non-linear, thereby ensuring a better accuracy. This also allows the user to set the required precision of the interpolation method to a desired value, that will be applied in the whole state space.

The mesh is generated using object-oriented programming in Python, where each cell (see Section 2.4.2) is an instance of a `Cell` object, that contains the cell coordinates, polynomial interpolation coefficients and cell number as attributes. Fig. 5 presents a flowchart of the corresponding algorithm. The –recursive– routine consists in creating an instance of a `Cell` object that will constitute the *whole* grid. The constructor is called with specified cell boundaries (which correspond, in the case of this first cell, to the state-space domain), an absolute error tolerance for the tabulated thermodynamic property and a cell number, by default set to 0 for this first cell. The constructor then calculates matrix A with Eq. (10) and if the cell is within the *validity* domain or overlapping it, an interpolation error is approximated. Note at this stage the difference between: (i) the state space formed by the ($\rho - e$) couple used to compute a third quantity, and (ii) the validity domain, that is the space in which one ensures an interpolation up to the required accuracy (in this work in the ($p - h$) state space). The interpolation error is

computed by taking the maximum absolute error over 9 verification points that are located in between the 16 passage points (see the gray dots in Fig. 4). If the error is higher than the specified tolerance (chosen by the user), the cell is subdivided into 4 sub-cells. The constructor is then called recursively on each `Cell` object, and the 4 sub-cells (blue dash lines in Fig. 4) are instantiated as attributes of the current `Cell`; for each of those 4 cells, the constructor is called with a halved range, the same tolerance and a new unique cell number. This process goes until the tolerance criterion is met, then the `Cell` data is stored in an external text file. Each line of the text file corresponds to a cell and is composed of the cell number, its x and y boundaries in the state space, the 16 polynomial coefficients and the 4 sub-cell numbers. If the cell is at the bottom of the tree, there are no sub-cells and -1 is stored instead, which acts as a flag for the later reading process. This method essentially constitutes a quad-tree algorithm, used to find the adequate cell in which the point of interest is located (in the state space) during the actual CFD. When the cell at the bottom of the tree is reached, the 16 bicubic polynomial coefficients are retrieved and the function is calculated.

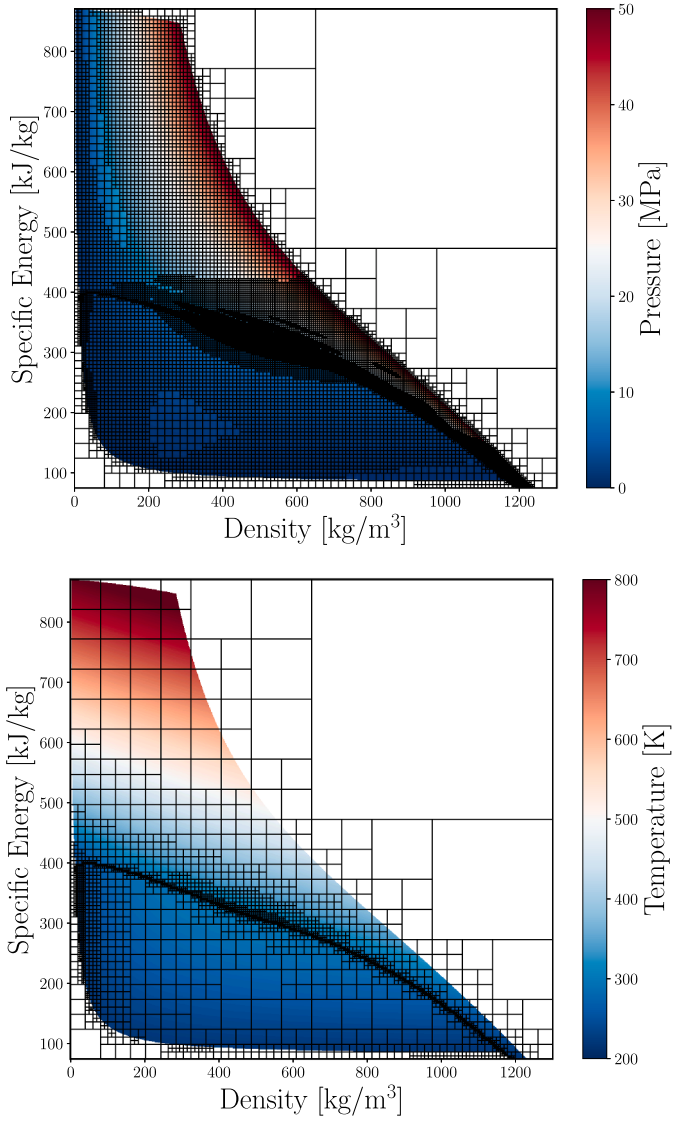

Fig. 6. Properties in the $\rho - e$ state space and mesh generated by the tabulation algorithm. The imposed precision for the tables is 0.1 [Pa] for pressure and 0.0001 [K] for temperature.

2.4.4. Limitations and fallback methods

Because the thermodynamic relations provided by `COOLPROP/REFPROP` are not always able to provide a solution, e.g., near the critical point, the algorithm should be able to handle such cases without storing non-physical values. The strategy adopted in the present work is twofold: (i) if no value can be computed at any of the 16 interpolation points within the cell, this current cell is deleted and the lookup table falls back on the upper cell, though the precision criterion may not be met; (ii) if some values can be computed but not for all of the 16 interpolation points, the cell is further subdivided unless no values can be computed in one of its 4 sub-cells (i.e., case (i)). In addition, because there can be quite high gradients near the saturation line, one can also choose to relax the error tolerance if the cell dimensions are getting below a certain threshold, in order to avoid building a prohibitively large lookup table.

Even though those strategies relax the error tolerance, the error is located in a very small range of the state space, often located in the near vicinity of the critical point. The actual error of the generated table is thus checked a posteriori in the following section to ensure that it stays reasonable in said region. In addition, note that during the CFD simulation itself, some thermodynamic states may pass through the region of less accuracy, but usually only during the convergence process.

2.5. Initial and boundary conditions and numerical procedure

Total quantities are prescribed at the inlet of the nozzle, i.e., the total inlet pressure p_{in} and the total inlet temperature T_{in}, whereas the (static) pressure is specified at the outlet. Note that the inlet and outlet boundary conditions are characteristic-based (non-reflective) so that spurious reflection waves do not interfere with/impede the convergence of the solution. In practice, this weak boundary condition allows the nozzle to become fully supersonic if the specified outlet pressure is below the minimum outlet pressure allowable by the physics at fixed inlet conditions. Because the experimental cases of Nakagawa et al. (2009) are fully supersonic, a low value for the outlet pressure of 0.8 [MPa] is specified, and never achieved in practice as the flow is supersonic a the outlet. A no-slip adiabatic (strong) boundary condition is applied at the wall. In addition, an extra set of boundary conditions for the quality is needed when using the HRM as Eq. (3) is added. For the inlet/outlet, the characteristic-based boundary condition is then applied to the quality (ρx). Note that there is no need to impose a boundary condition at the wall for the quality as there is no diffusion term in Eq. (3).

The interior of the domain (excluding the boundaries) is initialized using pressure and density values that must be specified by the user. The inputted density is also used with the pressure to calculate the state at the outlet during initialization. In addition, a Mach number is specified to initialize the velocity field required for the momentum and compute the total quantities at the inlet. In HRM, the quality is initialized to the equilibrium quality and the other (solution) variables are initialized with the converged HEM solution variables. The HRM simulation is then carried out until convergence.

At the beginning of each iteration of the solver, the tabulated EoS is used to compute primitive variables (e.g., p, T, etc.) as a function of the density and the specific internal energy. The solution is then moved forward in time and the EoS is used once again in preparation for the turbulence model. Lastly, the turbulence properties are integrated with time.

For HEM simulations, the CFL number is set to a constant value of 50 for 30 000 iterations, then to 5 for another 20 000 iterations in order to allow finer convergence/solution accuracy. The local time step is then computed in each cell based on this CFL, the local mesh size and velocity. For HRM simulations, slight modifications were made to the original implementation of the solver to set the CFL as a linear function of the quality, that is, $CFL = 0.05$ if $x = 0.0$ and $CFL = 0.5$ if $x \geq 0.5$. This is done because the system of PDEs becomes stiff as the quality

tends towards zero (large speed of sound compared to advection velocity in the incompressible limit). Thus, the solution is propagated more quickly in the regions with higher qualities, where the relaxation process modeled by the HRM is less important. In most of the divergent part of the nozzle (far from the throat), $CFL \approx 0.5$, which contributes to accelerate the convergence process. By doing so, it was found that a solution could be obtained with roughly 5.10^6 iterations. The convergence criterion that is used is based on the conservation of the mass flow rate through the device; the solution is considered converged when the relative difference of mass flow rates between inlet and outlet steadily fell below 5.10^{-3}.

The entirety of the computation is performed on the Digital Research Alliance clusters in Canada. Each case ran on a single computation node that is comprised of 40 Intel Skylake cores operating at 2.4 GHz.

2.6. Mesh grid

The 2D mesh (Fig. 1) is generated using `GMSH` and refined at the wall to ensure a maximum wall coordinate $y^+ \approx 1$, a prerequisite for the $k-\omega$ SST closure. As shown in Fig. 1, the structured mesh is also refined near the vicinity of the throat in order to better capture the compressible phenomena. As the simulation is 2D, a total of 163 304 quadrilateral elements is used for each of the three geometries and the mesh independence is verified by comparing the simulation results of the regular mesh with the ones obtained using a mesh with twice as many elements in the axial direction. The two mesh grids were found to lead to indistinguishable results.

3. Results and discussion

In this section, the accuracy of the tabulated EoS is verified and discussed, also with regards to the metastable properties that require special treatment. The simulation speed is compared to a previous algorithm and the solver is validated in HEM against nozzle pressure profiles. Lastly, the HRM and HEM results are compared and the phenomenology of mass flow rate increase in HRM is explained.

3.1. Tabulated thermodynamic relations

The most influential thermodynamic relations required by the solver are those to find the pressure and the temperature as a function of ρ and e, in order to close the system of PDEs. Therefore, one focuses, in this section, on the tables generated for those quantities for analysis and validation purposes. Fig. 6 displays the grids generated for pressure and temperature in the $(\rho - e)$ state space. The mesh for the pressure table was generated by imposing a maximum interpolation error of 0.1 [Pa] with relaxation to 0.1 [kPa] if the cell width (abscissa) is below 0.5 [kg/m^3]. Note that only the validity region was represented in the figure so that the region in white is outside of said validity region. The generated grid is composed of 175 637 cells/sub-cells elements and requires roughly 35 MB of RAM during the CFD simulation. One can notice that, as expected, the majority of the elements are present along the saturation curve. Additional refinement can also be noticed in the near vicinity of the critical point in the center of the domain as the pressure gradients with respect to ρ and e are high in that region. In addition, the pressure grid requires more elements in the region of low energy and high density. Indeed, in this region the fluid is in the liquid phase and the pressure varies quite strongly with both state variables. For the temperature table, the error tolerance is set to 0.0001 [K] with relaxation to 0.001 [K] with the same cell width threshold. Likewise, the grid is composed of 96 589 cells/sub-cells elements and requires roughly 20 MB of RAM during the CFD simulation.

As mentioned in Section 2.4.4, the tabulation algorithm contains some fallback mechanisms in order to prevent non-physical values or excessive refinement. This is why it is important to verify the interpolation error a posteriori. Fig. 7 displays the relative error, defined as:

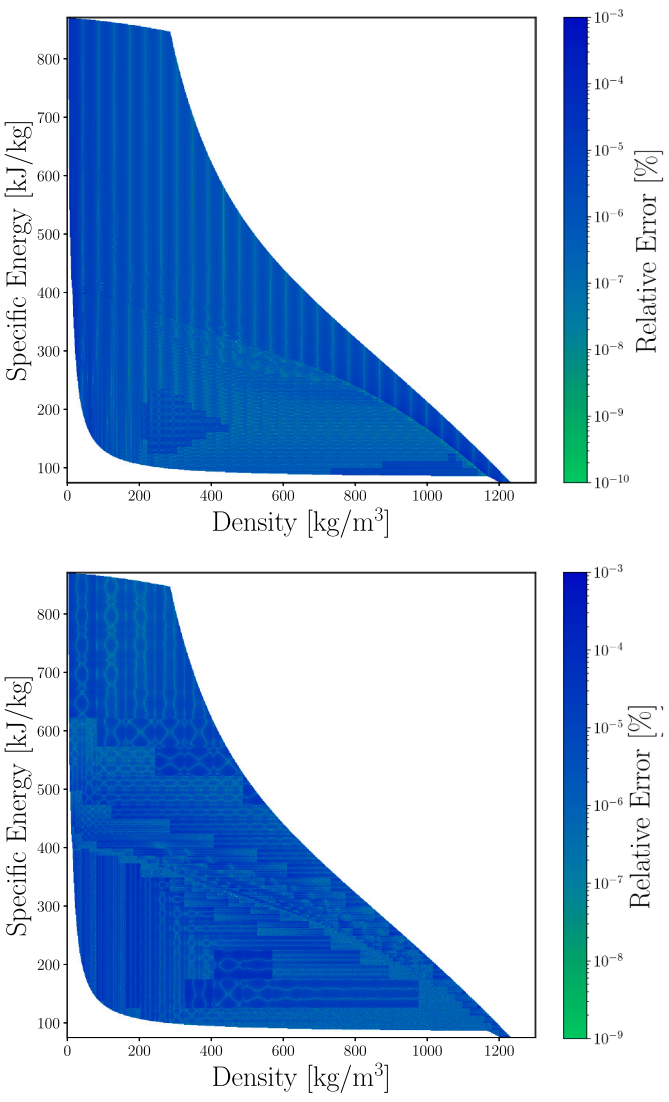

Fig. 7. Relatives errors in the $\rho - e$ state space.

$$\text{Relative Error} = \left| \frac{\chi_{interp} - \chi_{sol}}{\chi_{sol}} \right|, \tag{12}$$

for pressure and temperature. The plots were generated by taking 10^6 linearly spaced points in the $\rho - e$ state space. Again, only the validity range of the lookup table is shown. The relative error is mostly within the range $(10^{-5} - 10^{-9})$% for the pressure. Actually, the higher errors, of the order of 10^{-3}% are located in the very near vicinity of the saturation line. In practice, it is unlikely that the solution will contain a lower precision point, adding to the fact that said point still has a quite acceptable precision and won't prevent the solution from converging. Interestingly, some peculiar patterns can be observed in Fig. 7. Those are naturally occurring within each generated cell and are an image of the curvature of the bi-cubic interpolation function within that cell. Indeed, upon close attention, one can notice that the error tends towards zero at the location of the interpolation points (Fig. 4), where the error *is* by construction zero and curves around in between.

For HRM simulations, special care should be taken to compute the metastable properties. As per Fig. 2, the metastable properties required for the algorithm are $\rho_{ml}(p, e_{ml})$ and $T_{ml}(p, e_{ml})$. Metastable properties (obtained from the `REFPROP` library) can be calculated in the portion of

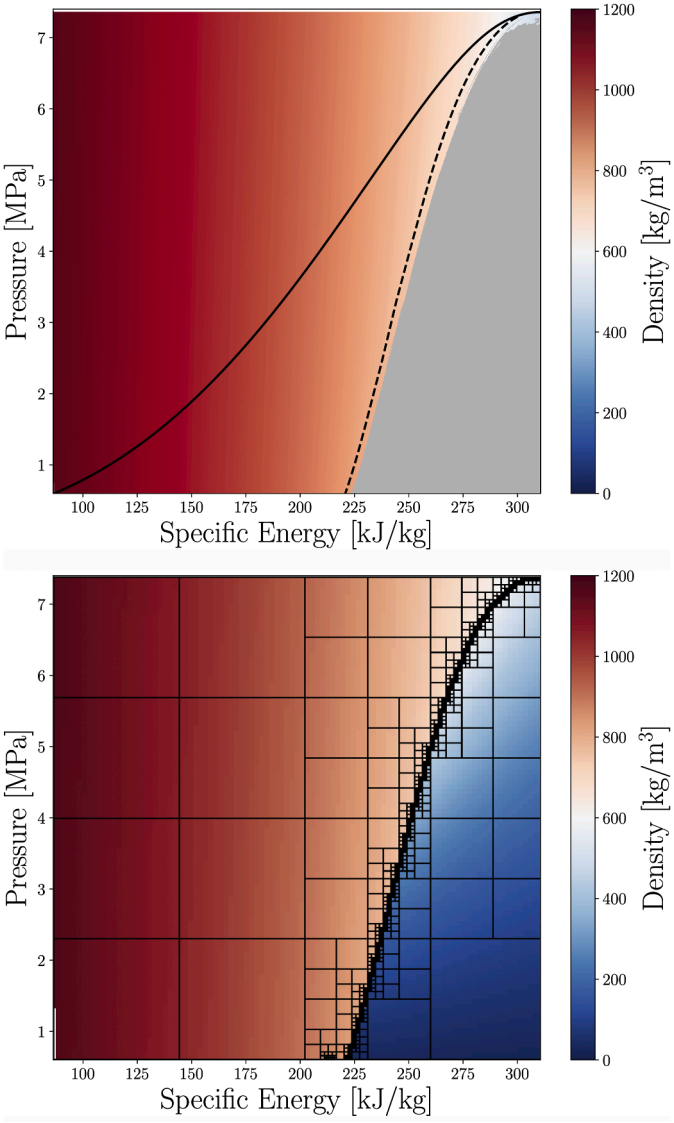

Fig. 8. Density in the $\rho - e$ state space including the metastable region. In Fig. 8a, the invalid states are represented in gray, and the saturation curve (plain curve) and the approximated spinodal limit (dashed curve) are plotted.

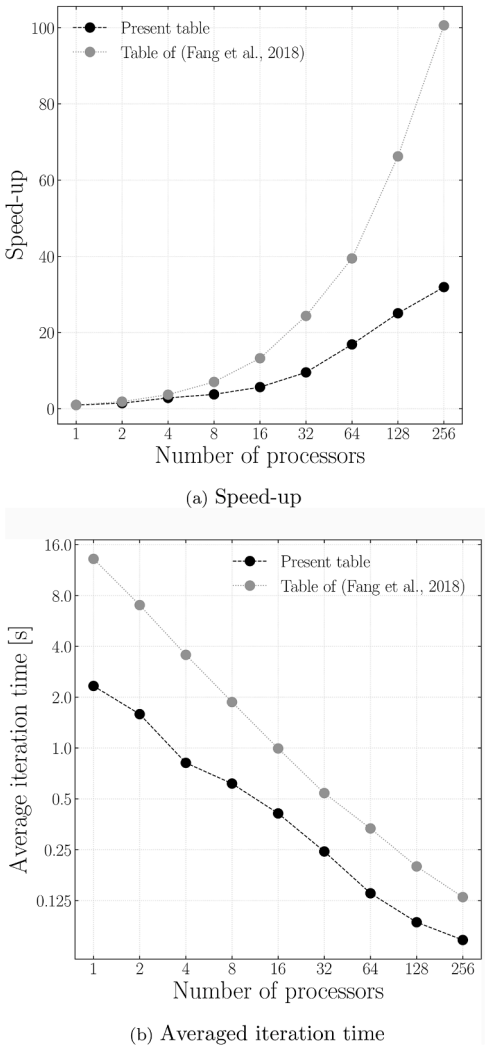

Fig. 9. Performance comparison between the present tabulated method and the one of Fang et al. (2018).

the thermodynamic state space comprised between the saturation curve and the *spinodal* limit, which is the limit beyond which a state becomes unstable. The spinodal limit can be expressed as the locus of thermodynamic states such that $\frac{\partial p}{\partial v}\Big|_T = 0$. Fig. 8a shows the raw metastable density retrieved from the library, with the gray region indicating failure to compute said property. The spinodal limit is then the limit of the predictable region (that is, the limit between colored and gray regions). Because the spinodal is not sharply defined, especially near the critical point (Fig. 8a), it is reconstructed (with a safety margin in the abscissa direction) by a spline function. The invalid (grayed) region is then set to the equilibrium value to construct the interpolation table, as seen in Fig. 8b. In practice (and for the results presented here), the properties are never retrieved from the reconstructed invalid region. Note also that only the left part (on the liquid side) of the spinodal limit has been considered, as the HRM is used to model *flashing* expansion processes only.

3.2. Table speed-up

To assess the performance of the novel tabulated method, the latter is compared to the tabulated method of Fang et al. (2018) for the test case of Nakagawa et al. (2009) (case c, Table 1). Fig. 9 shows the speed-up, defined as $t_{(1\ proc)}/t_{(n\ procs)}$, as well as the average iteration time as a function of the number of processors for both tables. Each simulation ran for 1000 iterations (on the converged solution) on the same cluster and the pre-processing time was not taken into account. The speed-up increases more rapidly when using the table of Fang et al. (2018), while the average iteration time is lower when using the present table (depending on conditions and number of CPUs, the present table is between 2 to 6 times faster). This indicates that the present tabulation method is indeed faster than the table of Fang et al. (2018) but that there is less computation time gain obtained from the parallelization process (which is also a confirmation of the efficiency of the current approach). Note that despite the tabulated method of Fang et al. (2018) being reported to perform roughly 66 times faster than the original Span-Wagner EoS for transcritical CO_2 applications, the tabulated equation of state constitutes the bottleneck in terms of simulation speed. The interested reader is invited to review the original article of Fang et al. (2018) for a thorough description of the algorithm. If the calculation time required by the EoS is reduced, the time gain obtained/obtainable is reduced as well (since the present algorithm performs faster, other parts of the code, not related to the EoS, may limit the speed-up). In practice, this means that adding more CPUs while using the table of Fang et al. (2018) will tend to compensate the low speed of the tabulated method, but it is not

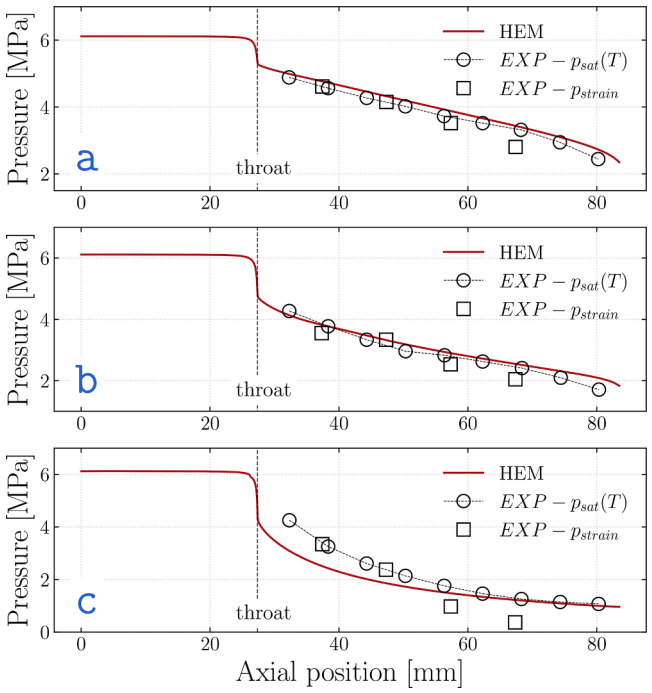

Fig. 10. Pressure profiles along the center-line of the nozzle (CFD) and comparison with the experimental data of Nakagawa et al. (2009). Please refer to Table 1 for geometrical and inlet parameters of cases a, b and c.

practical due to the finite amount of computational resources that is at disposition. Instead, the same simulations can be ran using significantly less resources with the present table.

3.3. Validation and verification of the solver

As demonstrated by Palacz et al. (2015) in the context of ejector flows, the validity of the HEM decreases as the expansion occurs at lower temperatures. In addition, it can be expected that the metastable liquid phase should be more present at lower nozzle pressures since the metastable properties range is larger at lower pressures (Fig. 8). Therefore, it was chosen in the present work to study the nozzle expansion at temperatures below critical (Table 1) from the experiments of Nakagawa et al. (2009). Fig. 10 displays the comparison of the present CFD-HEM results with the experimental measurements. Note that two separate methods were used to measure the pressure: (i) by measuring the wall temperature and deducing the pressure from saturation properties ($p_{sat}(T)$); (ii) by direct pressure measurement with strain gauge (p_{strain}). As reported in Nakagawa et al. (2009), small holes were drilled along the centerline of both nozzle side walls, with eleven holes on one side for thermocouple taps and four holes on the other side for the strain-gauge taps. Static temperatures and pressures were simultaneously measured through the taps. Measurements were performed when steady state was reached, which was determined based on the profiles of the experimental run. The interested reader is invited to review the original paper of Nakagawa et al. (2009) for detailed information about the experimental setup. Note that discrepancies between the two types of measurements may come from metastability effects, though it is the authors' understanding that the HRM might not be able to model those specific effects since, as discussed in Section 2.5, equilibrium conditions are expected at the wall. The measurements are then compared to the pressure at the center line of the nozzle, obtained from the converged HEM solution. Since the equilibrium is assumed (with HEM), there is no difference between the pressure field and the saturation pressure obtained from the temperature field ($p_{sat}(T)$). As seen in Fig. 10, the prediction of the HEM is fairly accurate for cases a and b. For case c, discrepancies between the HEM and the experimental

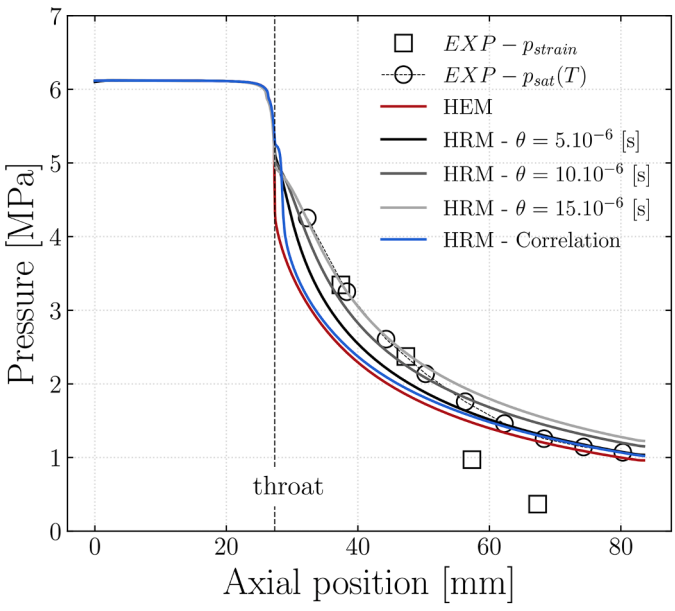

Fig. 11. Pressure profiles obtained for case c using HEM and HRM with different constant relaxation times and the correlation of Angielczyk et al. (2020), and comparison with experimental measurements (Nakagawa et al., 2009).

data are most visible in the first portion of the diffuser, where the simulation under-predicts the pressure. It was thus chosen to use case c to conduct the study on HRM and investigate the potential improvement of said model.

3.4. Homogeneous equilibrium vs homogeneous relaxation

As stated, the study presented in this section is conducted on case c (Tab. 1). Note also that as in the experiments of Nakagawa et al. (2009), the nozzle is fully choked. A parametric study is conducted to quantify and qualify the influence of the relaxation time on the local flow features as well as the mass flow rate within the nozzle. To this end, the results of the HEM simulations are compared to those of the HRM simulations performed with (i) three increasing relaxation times and (ii) the correlation of Angielczyk et al. (2010). Note again that other correlations exist for CO_2 in the literature such as in the works of Haida et al. (2018) or Log et al. (2024a), but those correlations have been found to yield relaxation times so high that the solution for the metastable properties is located in the unstable region for the investigated case: this also illustrates the lack of universality of such correlations. To the best of the authors' understanding, the value/correlation of θ is highly case-dependent and only the correlation of Angielczyk et al. (2010) was calibrated on the cases of Nakagawa et al. (2009), though on higher inlet pressure cases of 9.1 [MPa] and never tested on the cases presented in the present work.

3.4.1. Pressure and quality profiles

One can first observe the behavior of the pressure curves along the nozzle axis as the relaxation time is varied, as shown in Fig. 11. It is seen that consistent variation of θ leads to consistent modification of the pressure profile, that is, as the relaxation time is increased by steps of 5.10^{-6} [s], the pressure profile in the divergent (where the flow is two phase) is lifted by similar increments. Interestingly, it appears that a constant value of $\theta = 15.10^{-6}$ [s] fits best the first half of the divergent, but leads to an over-prediction in the second half, whereas the curve for $\theta = 5.10^{-6}$ [s] fits best the second portion of the divergent. One could then argue that varying θ from 15.10^{-6} [s] to 5.10^{-6} [s] along the expansion could yield an optimal fitting. However, the raised pressure profile is a consequence of the physics that takes place in the near

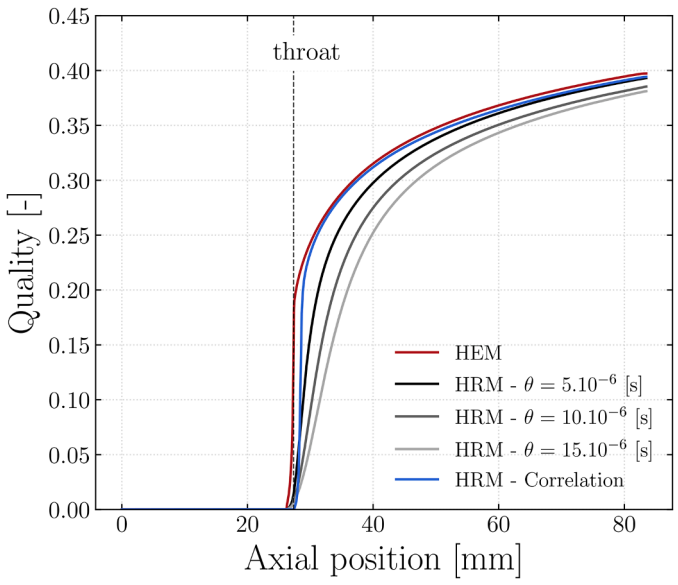

Fig. 12. Quality profiles obtained for case c using HEM and HRM with different constant relaxation times and the correlation of Angielczyk et al. (2020).

vicinity of the throat, where the metastability effects are most prominent and the relative difference of quality between HEM and HRM is most pronounced. In the second half of the divergent, the HEM and HRM pressures are actually very close to each other as the variation of the quality is low in that region. Thus, lowering θ along the divergent could not allow to recover a better fitting. In addition, one can see that the correlation of Angielczyk et al. (2010) yields little difference with the HEM solution and is not able to properly fit the experimental measurement. In fact, the relaxation time drops to extremely small values as the pressure gets lower (Eq. (6)) right after the throat location, which effectively creates a pressure shift in that very small region. Fig. 12 presents quality profiles along the center line of the nozzle. The effect of the relaxation time can there be seen, as it delays flashing by reducing the slope of the quality profile.

Note at this stage it is possible that the measurements in the work of Nakagawa et al. (2009) could have some flaws. Indeed, as $p_{sat}(T) \approx p_{strain}$ in the first part of the diffuser, the flow should be at equilibrium from the experimental point of view. However, in this area, the pressure values clearly agree with the HRM with a large relaxation time, i.e., with a significant non-equilibrium. Inversely, there is a difference in the measured pressures according to the two different methods in the second half of the diffuser, meaning that a growing non-equilibrium appears in this part. Nevertheless, the profile of $p_{sat}(T)$ agrees well with the HEM and it is also expected, from a physical point of view, that the non-equilibrium tends to damp out along the pipe as HEM and HRM predictions become closer. In addition, the present analysis, using the HRM, also indicates that the flow is at equilibrium at the wall (i.e., where the measurements are taken). This is verified in Fig. 13 by analyzing the relative difference of quality with respect to the equilibrium $(x_{eq} - x)/x_{eq}$ and the pressure profiles obtained from the pressure field p directly and via the temperature field ($p_{sat}(T)$). The profiles are plotted at the wall as well as at the center line for reference, and for two different values of the relaxation time. As one can see, the difference between quality and equilibrium quality is negligible at the wall, and the pressures profiles obtained using both methods are equal, indicating that the fluid is indeed at equilibrium at the wall. Moreover, one can see when comparing Fig. 13a and b that as θ is increased, the difference between p_{center} and $p_{sat}(T_{center})$ increases as well, whereas the wall seems to remain at equilibrium pressure. Likewise, with a higher θ, the relative difference of qualities in the centerline gets higher and extends further into the divergent, but seems to remain somewhat

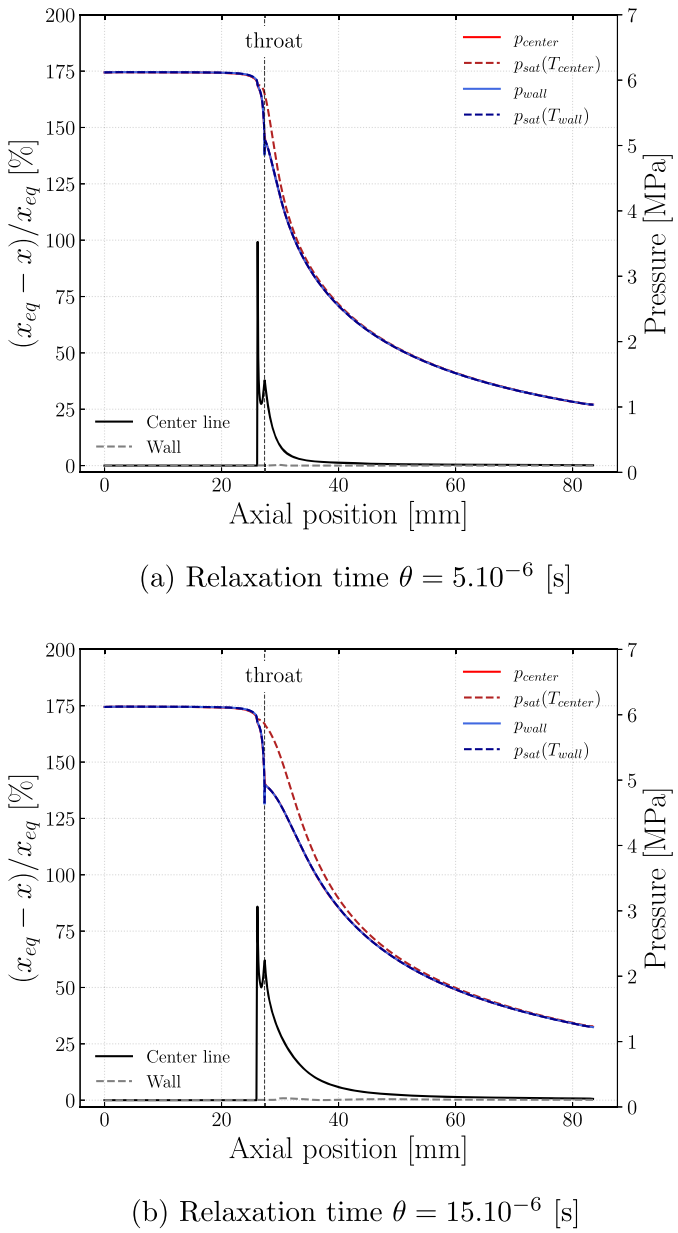

Fig. 13. Relative difference of quality with respect to the equilibrium and pressure profiles using different methods at the center line and at the wall for case c.

negligible at the wall. Note also that the pressure appears to be uniform at a given axial position. As stated in Section 3.3, the experimental measurements are done on the side walls, at the center line, and not at the upper/lower walls. Nonetheless, it is still expected, by the same logic, that the fluid will be at equilibrium at the side walls. This further encourages the authors to believe that the experimental pressure measurement should not be used to quantify the actual degree of non-equilibrium. The size of the holes to connect the pressure taps compared to the very small dimensions of the part (0.24 [mm] at the throat) is not provided, and possible heat transfer features are not discussed for the measurements of $p_{sat}(T)$ in Nakagawa et al. (2009).

3.4.2. *Local flow features and mass flow rates*

In this section, the local flow fields of velocity (Fig. 14) and density (Fig. 15) are compared, which allows to describe the mechanism leading to the increase of the mass flow rate in HRM, that is associated to two competing phenomena. On one hand, as seen in Fig. 14, increasing the

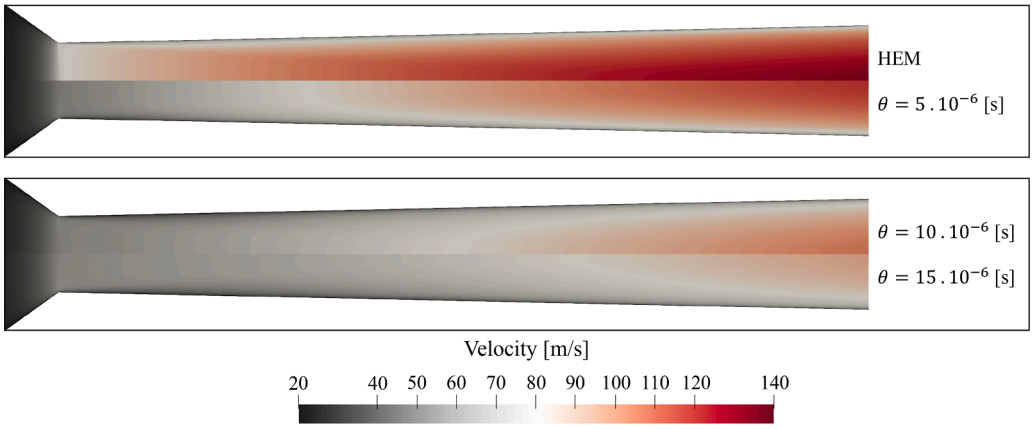

Fig. 14. Fields of the mean axial velocity component obtained for case C using HEM and HRM with different relaxation times. The geometry was stretched X4 in the vertical direction for better readability.

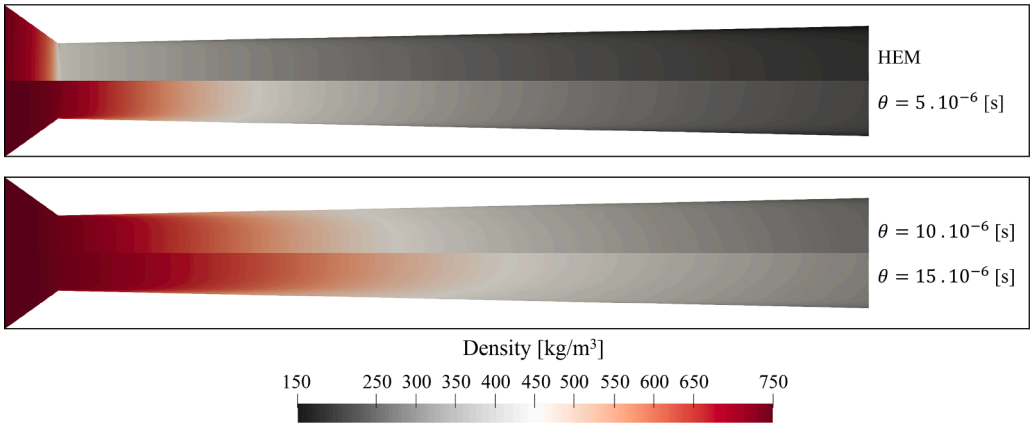

Fig. 15. Density fields obtained for case C using HEM and HRM with different relaxation times. The geometry was stretched X4 in the vertical direction for better readability.

relaxation time reduces the velocity in the divergent, which tends to decrease the mass flow rate. On the other hand, as shown in Fig. 15, increasing θ also results in the increase of the density, which increases the mass flow rate. Note that those observations are consistent with the ones obtained by Palacz et al. (2017) using their pressure-based solver to perform HRM simulations of ejectors. The competition of those two mechanisms, in the end, results in the increase of the mass flow rate with θ as the density effect is dominating. Table 2 summarizes the mass flow rate effects of the relaxation time for each case. The mass flow rate increase obtained with θ grows quickly to non-negligible values. In the case that fits best the pressure profile in the first portion of the diffuser (Fig. 11), i.e., $\theta = 15.10^{-6}$ [s], the mass flow rate is increased by more than 18%. Although no mass flow measurements were performed in the experiment (Nakagawa et al., 2009), one can appreciate metastability effects. As explained in De Lorenzo (2018), introducing instabilities generally leads to an increase in the speed of sound, which can increase the mass flow rate under choked conditions and modify the pressure profiles. However, as numerical models such as the present one do not include the whole flow physics and non-equilibria, discrepancies between numerical results and experimental measurements may still be expected.

Table 2
Mass flow rate and increase with respect to the HEM solution for case C with various relaxation times and the correlation of Angielczyk et al. (2010).

	Mass flow rate [g/s]	Increase w.r.t. HEM [%]
HEM	23.07	/
HRM - $\theta = 5.10^{-6}$ [s]	24.69	7.02
HRM - $\theta = 10.10^{-6}$ [s]	26.16	13.40
HRM - $\theta = 15.10^{-6}$ [s]	27.30	18.34
HRM - Correlation of Angielczyk et al. (2010)	23.19	0.52

4. Conclusions

In this work, two advances were made towards wall-resolved simulations of flashing CO_2 nozzles and ejectors. Firstly, a novel general method for the construction and interpolation of the equation of state was described. The method is based on bi-cubic functions and a quadtree algorithm with local refinement of the interpolation grid in the thermodynamic state-space. It was found that this method allows for both reasonable storage size of the tabulated properties and fast interpolation speed during the CFD simulations. Although the method is here used in the context of CO_2 only, it can be applied without modification to generate any table linking three thermodynamic properties for any fluid, given that the relation is obtainable from an external source (as in the present case, through the `REFPROP` and `COOLPROP` libraries). The table generation method is based on a provided absolute error tolerance, and it was verified a posteriori that the interpolation error is indeed below the required threshold.

Secondly, a density-based formulation of the HRM was implemented for the first time in a CFD frame and the impact of the relaxation time was studied by employing both constant values and the correlation of Angielczyk et al. (2010) that was calibrated on similar flashing CO_2

nozzle cases. The pressure and quality profiles within the device were found to behave in a consistent manner, also in agreement with regards to the current literature. It was observed that as a constant relaxation time was increased, the pressure profiles in the fully supersonic nozzle were shifted upward and the jump in the quality profiles was smoothed, inducing a delay in the flashing process. In addition, the mass flow rates increased significantly, accounting for more than 18 % when the pressure profile is best fitted by the HRM in the near-throat region. It was also found that the best fit with constant relaxation time in the first half of the diffuser over-predicted the pressure in the second half, and that a lower relaxation time was best in that region.

Nonetheless, the study indicates that the metastability effects in HRM are mostly occurring in the near vicinity of the throat (i.e., where flashing occurs), and therefore the worse pressure fitting in the second half of the diffuser was essentially a consequence of the delay in the first half of the diffuser. This is confirmed by the results obtained with the correlation of Angielczyk et al. (2010) for the relaxation time, where the latter takes non-negligible values only in a very small region near the throat, leading nonetheless to a similar rise of the pressure profile downstream. Said correlation yielded poor results with no significant mass flow rate increase, which may indicate that the required value of the relaxation time is highly case dependent and that it is unlikely that one may find a universal law for the current HRM framework. Furthermore, it is the understanding of the authors that only a correlation including negative relaxation times would allow pressure fitting along the entirety of the nozzle, where one would have positive (physical) relaxation times in the first portion of the diffuser, decreasing to reach negative (non-physical) values downstream to counteract the pressure rise induced upstream. This may indicate that some physics is missing in the HRM. Therefore, it could be interesting, in future works, to re-introduce the saturated-liquid phase lacking in the current HRM framework to develop a new hybrid model. Lastly, one may point out the crucial lack of quality experimental measurements (pressure and temperature profiles, mass flow rates) that are needed in order to fully understand what phenomena are at play within flashing CO_2 nozzles and ejectors.

Declaration of competing interest

The authors declare that they have no known competing financial interests or personal relationships that could have appeared to influence the work reported in this paper.

Acknowledgements

The NSERC chair on industrial energy efficiency established in 2019 with the support of Hydro-Québec, Natural Resources Canada (CanmetEnergy-Varennes) and Copeland are here gratefully acknowledged. All calculations have been done using the HPC facilities of the Digital Research Alliance of Canada.

References

Abas, N., Kalair, A.R., Khan, N., Haider, A., Saleem, Z., Saleem, M.S., 2018. Natural and synthetic refrigerants, global warming: a review. Renew. Sustain. Energy Rev. 90, 557–569.

Ameli, A., Afzalifar, A., Turunen-Saaresti, T., 2017. Non-equilibrium condensation of supercritical carbon dioxide in a converging-diverging nozzle. J. Phys. Conf. Ser. 821 (012025), 1–10.

Angielczyk, W., Bartosiewicz, Y., Butrymowicz, D., 2020. Development of delayed equilibrium model for CO_2 convergent-divergent nozzle transonic flashing flow. Int. J. Multiphase Flow 131 (103351).

Angielczyk, W., Bartosiewicz, Y., Butrymowicz, D., Seynhaeve, J.-M., 2010. 1-D modeling of supersonic carbon dioxide two-phase flow through ejector motive nozzle. International Refrigeration and Air Conditioning Conference, pp. 1–8.Purdue

ANSYS, 2023. Ansys Fluent - CFD Software | ANSYS.

Bell, I.H., Wronski, J., Quoilin, S., Lemort, V., 2014. Pure and pseudo-pure fluid thermophysical property evaluation and the open-source thermophysical property library CoolProp. Ind. Eng. Chem. Res. 53 (6), 2498–2508.

Besagni, G., 2019. Ejectors on the cutting edge: the past, the present and the perspective. Energy 170, 998–1003.

Bilicki, Z., Kestin, J., Stuart, J.T., 1990. Physical aspects of the relaxation model in two-phase flow. Proc. R. Soc. London A Math. Phys. Sci. 428 (1875), 379–397.

Brown, S., Martynov, S., Mahgerefteh, H., Chen, S., Zhang, Y., 2014. Modelling the non-equilibrium two-phase flow during depressurisation of CO_2 pipelines. Int. J. Greenhouse Gas Control 30, 9–18.

Croquer, S., Poncet, S., Aidoun, Z., 2016. Turbulence modeling of a single-phase R134a supersonic ejector. Part 1: numerical benchmark. Int. J. Refrig. 61, 140–152.

De Lorenzo, M., 2018. Modelling and Numerical Simulation of Metastable Two-Phase Flows. Université Paris Saclay. Ph.D. thesis.

De Lorenzo, M., Lafon, P., Di Matteo, M., Pelanti, M., Seynhaeve, J.-M., Bartosiewicz, Y., 2017. Homogeneous two-phase flow models and accurate steam-water table look-up method for fast transient simulations. Int. J. Multiphase Flow 95, 199–219.

Downar-Zapolski, P., Bilicki, Z., Bolle, L., Franco, J., 1996. The non-equilibrium relaxation model for one-dimensional flashing liquid flow. Int. J. Multiphase Flow 22 (3), 473–483.

Fang, Y., 2019. Advanced Numerical Simulations of Two-Phase CO_2 Ejectors. Université de Sherbrooke.

Fang, Y., De Lorenzo, M., Lafon, P., Poncet, S., Bartosiewicz, Y., 2018. An accurate and efficient look-up table equation of state for two-phase compressible flow simulations of carbon dioxide. Ind. Eng. Chem. Res. 57 (22), 7676–7691.

Fang, Y., Poncet, S., Nesreddine, H., Bartosiewicz, Y., 2019. An open-source density-based solver for two-phase CO_2 compressible flows: verification and validation. Int. J. Refrig. 106, 526–538.

Flexi, 2023. Flexi Description and source code | Flexi.

Föll, F., Hitz, T., Mueller, C., Munz, C.-D., Dumbser, M., 2019. On the use of tabulated equations of state for multi-phase simulations in the homogeneous equilibrium limit. Shock Waves 29, 769-793.

Giacomelli, F., Mazzelli, F., Banasiak, K., Hafner, A., Milazzo, A., 2019. Experimental and computational analysis of a R744 flashing ejector. Int. J. Refrig. 107, 326–343.

Giacomelli, F., Mazzelli, F., Milazzo, A., 2016. Evaporation in supersonic CO_2 ejectors: analysis of theoretical and numerical models. 9th International Conference on Multiphase Flow.Firenze

Haida, M., Smolka, J., Hafner, A., Palacz, M., Banasiak, K., Nowak, A.J., 2018. Modified homogeneous relaxation model for the R744 trans-critical flow in a two-phase ejector. Int. J. Refrig. 85, 314–333.

Kim, M.-H., Pettersen, J., Bullard, C.W., 2004. Fundamental process and system design issues in CO_2 vapor compression systems. Prog. Energy Combust. Sci. 30 (2), 119–174.

Lamberts, O., 2018. Choking and Mixing Phenomena in Supersonic Ejectors.. Université Catholique de Louvain.

Lamberts, O., Chatelain, P., Bartosiewicz, Y., 2018. Numerical and experimental evidence of the Fabri-choking in a supersonic ejector. Int. J. Heat Fluid Flow 69, 194–209.

Lemmon, E.W., Huber, M.L., McLinden, M.O., 2010. NIST Standard Reference Database 23: Reference Fluid Thermodynamic and Transport Properties - REFPROP, 9.0 ed. Gaithersburg.

Liu, F., Groll, E.A., Li, D., 2012. Investigation on performance of variable geometry ejectors for CO_2 refrigeration cycles. Energy 45 (1), 829–839.

Log, A.M., Hammer, M., Deng, H., Austegard, A., Hafner, A., Munkejord, S.T., 2024. Depressurization of CO_2 in a pipe: effect of initial state on non-equilibrium two-phase flow. Int. J. Multiphase Flow 170, 104624.

Log, A.M., Hammer, M., Munkejord, S.T., 2024. A flashing flow model for the rapid depressurization of CO_2 in a pipe accounting for bubble nucleation and growth. Int. J. Multiphase Flow 171, 104666.

Lucas, C., Rusche, H., Schroeder, A., Koehler, J., 2014. Numerical investigation of a two-phase CO_2 ejector. Int. J. Refrig. 43, 154–166.

Menter, F.R., 1994. Two-equation eddy-viscosity turbulence models for engineering applications. AIAA J. 32 (8), 1598–1605.

Nakagawa, M., Berana, M.S., Kishine, A., 2009. Supersonic two-phase flow of CO_2 through converging–diverging nozzles for the ejector refrigeration cycle. Int. J. Refrig. 32 (6), 1195–1202.

Palacios, F., Colonno, M., Aranake, A., Campos, A., Copeland, S., Economon, T., Lonkar, A., Lukaczyk, T., Taylor, T., Alonso, J., 2013. Stanford university unstructured (SU2): An open-source integrated computational environment for multi-physics simulation and design. 51st AIAA Aerospace Sciences Meeting including the New Horizons Forum and Aerospace Exposition 2013.Grapevine, USA

Palacz, M., Haida, M., Smolka, J., Nowak, A.J., Banasiak, K., Hafner, A., 2017. HEM and HRM accuracy comparison for the simulation of CO_2 expansion in two-phase ejectors for supermarket refrigeration systems. Appl. Therm. Eng. 115, 160–169.

Palacz, M., Smolka, J., Fic, A., Bulinski, Z., Nowak, A.J., Banasiak, K., Hafner, A., 2015. Application range of the HEM approach for CO_2 expansion inside two-phase ejectors for supermarket refrigeration systems. Int. J. Refrig. 59, 251–258.

Quinn, D., Stannard, D., Edwards, J., Botros, K.K., Johansen, C., 2022. Experimental visualization and characteristics of bubble nucleation during rapid decompression of supercritical and subcooled carbon dioxide. Int. J. Press. Vessels and Pip. 195, 104569.

Raman, S., Kim, H., 2018. Solutions of supercritical CO_2 flow through a convergent-divergent nozzle with real gas effects. Int. J. Heat Mass Transf. 116, 127–135.

Ringstad, K.E., Allouche, Y., Gullo, P., Ervik, A., Banasiak, K., Hafner, A., 2020. A detailed review on CO_2 two-phase ejector flow modeling. Therm. Sci. Eng. Prog. 20, 100647.

Roe, P., 1981. Approximate Riemann solvers, parameter vectors, and difference schemes. J. Comput. Phys. 43 (2), 357–372.

Rubino, A., Pini, M., Kosec, M., Vitale, S., Colonna, P., 2018. A look-up table method based on unstructured grids and its application to non-ideal compressible fluid dynamic simulations. J. Comput. Sci. 28, 70–77.
Smolka, J., Bulinski, Z., Fic, A., Nowak, A.J., Banasiak, K., Hafner, A., 2013. A computational model of a transcritical R744 ejector based on a homogeneous real fluid approach. Appl. Math. Model. 37 (3), 1208–1224.
Span, R., Wagner, W., 1996. A new equation of state for carbon dioxide covering the fluid region from the triple-point temperature to 1100 K at pressures up to 800 MPa. J. Phys. Chem. Ref. Data 25 (6), 1509–1596.